ADVANCED MATERIALS
www.advmat.de

High-Quality Black Phosphorus Atomic Layers by Liquid-Phase Exfoliation

*Poya Yasaei, Bijandra Kumar, Tara Foroozan, Canhui Wang, Mohammad Asadi, David Tuschel, J. Ernesto Indacochea, Robert F. Klie, and Amin Salehi-Khojin**

2D nanomaterials such as graphene and transition metal dichalcogenides (TMDCs) have shown outstanding potential in many fields such as flexible electronics,[1] sensing,[2,3] and optics,[4] due to their desirable physical and structural properties.[5–7] Among these materials, graphene has the highest charge carrier mobility,[8] but absence of a bandgap limits its practice in many applications.[9] On the other hand, molybdenum disulfide (MoS_2) atomic layers offer a noticeable bandgap resulting in extraordinary on/off ratios (>10^8),[10] but the material suffers from moderate charge carrier mobility.[11] Recent discovery of black phosphorus (BP) atomic layers (called phosphorene) holds promise to be widely used as an alternative 2D semiconductor in many areas of electronics and optoelectronics, owing to its high mobility,[12–14] tunable direct bandgap,[14–16] large on/off ratios (>10^5),[13,14] and anisotropic properties.[13,17,18] However, most of the studies on BP atomic layers so far[12–15,19–21] have used the mechanical exfoliation technique, which is only suitable for laboratory level demonstrations. To harvest the material's excellent properties, it is essential to employ scalable techniques to produce large quantities of exfoliated nanoflakes. In this report, we employed the liquid-phase exfoliation technique to produce highly crystalline atomically thin BP nanoflakes in the solution form by using ultrasonic energy as a source to break down the inter-layer van der Waals forces in appropriate solvents (see Experimental Section).

We surveyed several solvents from different chemical families such as alcohols, chloro-organic solvents, ketones, cyclic or aliphatic pyrrolidones, *N*-alkyl-substituted amides, and organosulfur compounds, covering a wide range of surface tensions (21.7–42.78 dyne cm^{-1}) and polar interaction parameters

P. Yasaei, Dr. B. Kumar, M. Asadi, Prof. A. Salehi-Khojin
Department of Mechanical and Industrial Engineering
University of Illinois at Chicago
Chicago, IL 60607, USA
E-mail: salehikh@uic.edu
T. Foroozan, Prof. J. E. Indacochea
Department of Civil and Materials Engineering
University of Illinois at Chicago
Chicago, IL 60607, USA
C. Wang, Prof. R. F. Klie
Department of Physics
University of Illinois at Chicago
Chicago, IL 60607, USA
D. Tuschel
HORIBA Scientific
HORIBA Scientific Inc.
Edison, NJ 08820, USA

DOI: 10.1002/adma.201405150

(2.98–9.3 $MPa^{1/2}$), and examined their performance for BP exfoliation (see Section S1, Supporting Information). Initially, a chunk of black phosphorous crystal (0.02 mg mL^{-1}) was immersed into different solvents and was sonicated for 15 h (total input energy – 1 MJ). We noticed that aprotic and polar solvents such as dimethylformamide (DMF) and dimethyl sulfoxide (DMSO) are appropriate solvents for the synthesis of atomically thin BP nanoflakes and can produce uniform and stable dispersions after the sonication (see Section S2, Supporting Information). The solutions were then centrifuged and their supernatants were carefully collected by a pipette. **Figure 1**A shows the BP nanoflake dispersions in DMSO and DMF after sonication for 15 h (left image) and after the centrifugation (right image), having concentrations up to 10 µg mL^{-1} (see Experimental Section).

As suggested by experimental[15] and theoretical[16,17] reports, BP atomic layers have a thickness dependent direct bandgap ranging from ≈0.3 eV in bulk to more than 1 eV in monolayer. Typically, optical absorption spectroscopy is a robust and reliable method to determine the bandgap of semiconductors in solution form. We used this technique to characterize our dispersed nanoflakes in DMF and DMSO solutions with a focus on the near-IR (NIR) range (Wavelength of 830–2400 nm) where the peaks associated with the optical band gap of atomically thin BP nanoflakes are likely to occur. Interestingly, in both DMF and DMSO solutions several spectral peaks were observed in the NIR range at ≈1.38, ≈1.23, ≈1.05, ≈0.85, and ≈0.72 eV (labeled as numbers 1–5 in Figure 1B) which are believed to be associated with the enhanced light absorption by mono-, to five-layers thick BP nanoflakes, respectively. These results are in a good agreement with the position of photoluminescence peaks reported for mono- to five-layers thick BP flakes obtained by mechanical exfoliation.[12,22] The smaller peaks at 1.38 and 1.23 eV compared to other peaks implies that the yields of mono- and bilayers are lower than other atomic layers.

We also measured the normalized absorption intensity over the characteristic length of the cell (A/l) at $\lambda = 1176$ nm ($E = 1.05$ eV) for DMF and DMSO solutions at different concentrations (C). As suggested by the Lambert–Beer law ($A/l = \alpha C$, where α is the extinction coefficient), a linear trend was observed for A/l versus concentration (Figure 1C), suggesting well-dispersed nanoflakes in both solutions. The extinction coefficients for DMF and DMSO solutions were extracted to be $\alpha = 4819$ and 5374 mL mg^{-1} m^{-1}, respectively. The BP flake size distribution was also analyzed by dynamic light scattering (DLS) spectroscopy and the average flake sizes were determined to be ≈190 and ≈532 nm for the DMF and DMSO solutions, respectively (Figure 1D).

 © 2015 WILEY-VCH Verlag GmbH & Co. KGaA, Weinheim

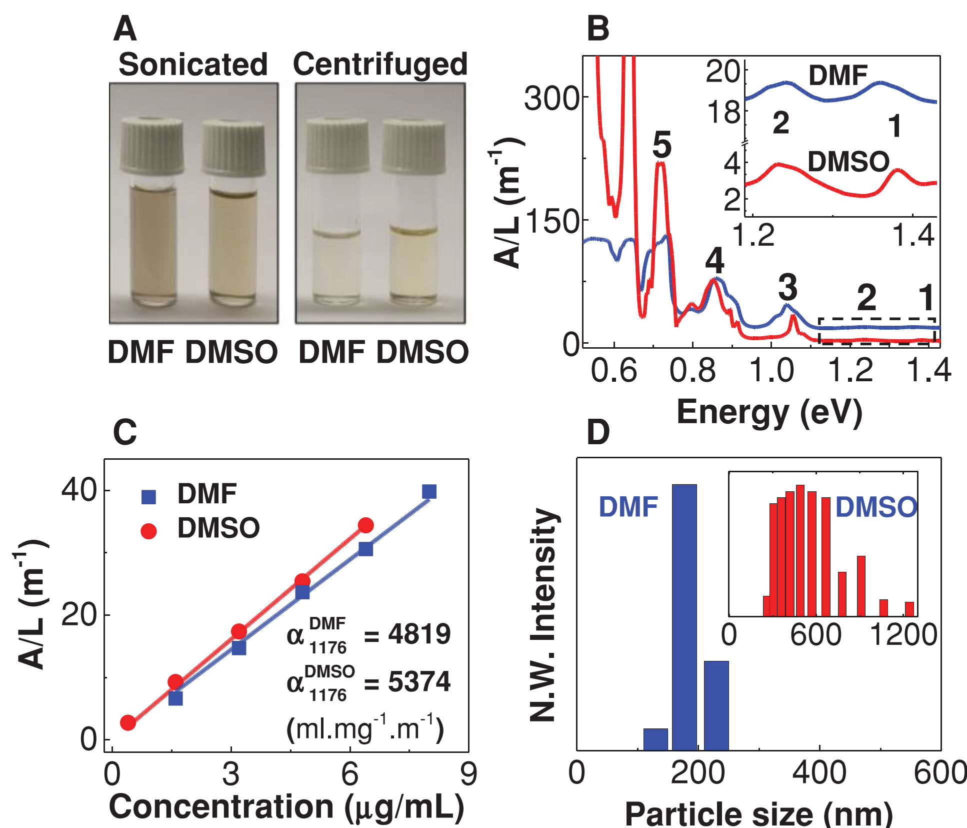

Figure 1. Solution level characterization of liquid-phase-exfoliated BP nanoflakes. A) Photograph of the atomically thin BP dispersions in DMSO and DMF solvents after sonication (left) and after centrifugation and supernatant collection (right). B) Optical absorption spectra obtained from dispersed BP nanoflakes in DMSO and DMF solvents. Five peaks indicated by numbers 1–5 correspond to the optical bandgap of mono- to five-layers BP nanoflakes. C) Normalized absorbance intensity over characteristic length of the cell (A/l) at different concentrations for $\lambda = 1176$ nm ($E = 1.05$ eV). The extinction coefficient (α) is extracted by linear fitting and can be used to estimate concentration of the subsequent solutions. D) DLS histogram for DMSO and DMF solution.

For further characterizations on isolated flakes, we used the "on chip separation method" in which the flakes remain on the surface in a circular pattern, due to the "coffee-ring effect"[23] (**Figure 2**A). Higher-magnification scanning electron microscopy (SEM) images show that the central area of the coffee rings is densely packed by randomly oriented atomically thin BP nanoflakes (Figure 2B), while individual flakes can be easily found near the outer peripheral regions (Figure 2D). We collected Raman point spectra from the individual flakes and obtained typical A_g^1 (out-of-plane mode), B_{2g} and A_g^2 (in-plane modes) BP peaks at wavenumbers of ≈360, ≈437, and ≈466 cm^{-1}, respectively (Figure 2C). The peak positions are consistent with the signature Raman spectrum of the mechanically exfoliated BP flakes, suggesting that the flakes are crystalline after the exfoliation.[21] To investigate the anisotropic structure of the exfoliated flakes, we performed angle resolved Raman spectroscopy experiments with a linearly polarized laser light. Figure 2C (left) shows the Raman point spectra obtained from an individual BP flake at different sample orientations. Similar to mechanically exfoliated flakes,[19,22,24] we observed that the intensities of the three vibrational modes strongly depend on the orientation of the sample. Figure 2C (right) shows the trend of A_g^1 and A_g^2 modes in 180° rotation of the sample. According to structure of the BP, the A_g modes are expected to be maximized when the laser polarization is aligned parallel to the X-axis of the crystal.[22] This can be used as a facile method to determine the crystalline orientation of the flakes.[22]

The thickness distribution of the flakes produced in DMF and DMSO solutions was systematically investigated by performing atomic force microscopy (AFM) height measurements. Figure 2D,E are SEM and AFM images of a randomly selected region showing a variation in the thickness of the flakes ranging from 5.8 to 11.8 nm (Figure 2E). Figure 2F represents the histogram of the flake thickness distributions in DMF and DMSO solutions obtained from height profiles of 70 individual flakes. In the case of DMF, >20% of the probed flakes are thinner than 5 nm, while in DMSO the flake thicknesses are most frequently in the range of 15–20 nm. Considering its higher yield of atomic layers, we chose DMF for the rest of characterizations.

Next, we performed transmission electron microscopy (TEM) characterization of the BP nanoflakes to study their crystallinity, quality, and number of layers (see Experimental Section and Section S4, Supporting Information). **Figure 3**A shows a typical TEM image of a BP nanoflake on a lacy carbon support. We used the fast Fourier transform (FFT) to identify the nanoflakes of BP with thicknesses down to a single layer. As theoretically suggested,[21] the intensity ratio of the (110) to (200) diffraction peaks (I_{110}/I_{200}) is greater than one

© 2015 WILEY-VCH Verlag GmbH & Co. KGaA, Weinheim

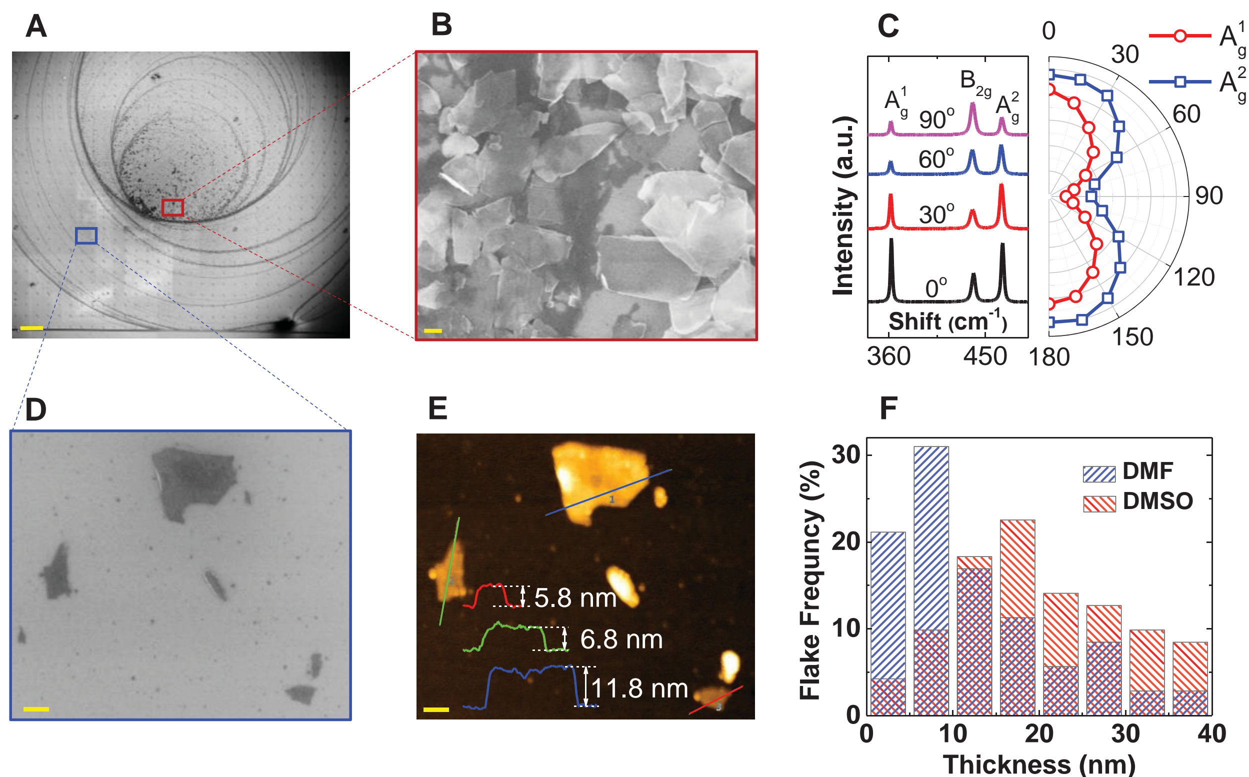

Figure 2. Morphological and Raman characterization of the synthesized BP nanoflakes. A) Low magnification SEM image of deposited nanoflakes on SiO_2/Si substrate, showing the "coffee-ring" structure (scale bar is 200 µm). B) Magnified SEM image of the central area of the rings (scale bar is 200 nm). C) Raman spectra of exfoliated BP nanoflakes at different orientations relative to the incident laser polarization. Three distinct spectral peaks were observed at ≈360, ≈437, and ≈466 cm^{-1}, which correspond to the A_g^1, B_{2g}, and A_g^2 BP peaks, respectively. The left image shows four spectra obtained from an individual flake in different orientations. The right image shows the orientation dependent A_g^1 and A_g^2 peak intensities. The strong variation in the peak intensity corresponds to anisotropic crystalline structure of the exfoliated flakes. D) SEM image of individual BP nanoflakes located at the outer region of coffee rings (scale bar is 200 nm). E) AFM image of the same area (shown in (D)), and their height profiles (inset) corresponding to the drawn lines (same colors). F) Statistical flake thickness distribution measured by AFM on 70 flakes, obtained from DMF and DMSO solutions produced in identical experimental conditions.

for monolayer and smaller than one for multilayer. So far, this ratio has only been experimentally verified for multilayers.[21] In our images, the I_{110}/I_{200} ratio is measured to be 2.7 ± 0.2, in good agreement with the computational value of 2.557[21] for monolayer BP (see Section S4.3, Supporting Information). In Figure 3B, the FFT patterns of different selected areas on different locations show identical features, suggesting the existence of a single crystalline, monolayer BP nanoflake over the whole image.

The atomic structure of the monolayer BP is resolved in Figure 3C using high-resolution TEM imaging. We also performed TEM simulations (viewing from the (001) direction) on mono- and multilayers BP structures using the well-known BP lattice parameters.[25] In the case of a monolayer, our simulated image has a hexagonal structure similar to graphene, while multilayers exhibit orthogonal structure due to ABA stacking order in >1 layers (see Figure S8, Supporting Information). The lattice parameters of simulated monolayer structure and imaged flake perfectly matched, further confirming the existence of monolayers. TEM image simulation (upper right inset) and a filtered section of the acquired image (lower left inset) are added to Figure 3C for comparison.

The quality of the BP nanoflakes is analyzed by performing energy-dispersive X-ray spectroscopy (EDX) analysis, as well as electron energy loss spectroscopy (EELS). The EDX result (Figure S10, Supporting Information) shows that the flakes only consist of phosphorous, without any noticeable impurity components. EELS elemental mapping also shows that an entire flake is only made of phosphorous atoms (Figure 3D). The near-edge fine structures of the phosphorous $L_{2,3}$ edges confirm the presence of pristine phosphorous and absence of the signature P_xO_y peak loss (Figure 3E).[19] By repeating the EELS analysis on the flakes obtained from aged solution (1 month), it was interestingly revealed that flakes remain intact in solution form. Panels A, B, and D of Figure 3 are taken from different flakes.

The electronic properties of individual BP nanoflakes were characterized in a back-gated field-effect transistor (FET) platform. **Figure** 4A shows the false color SEM image of a typical fabricated device with a flake thickness of ≈7.4 nm as measured by AFM (Figure 4B). Figure 4C shows the logarithmic scale current versus back-gate voltage (I_{SD} vs V_{BG}) characteristics of the device in ambient conditions at constant source-drain bias (V_{SD}) of 0.7 and 1.3 V. Using the linear slope of the I_{SD}

© 2015 WILEY-VCH Verlag GmbH & Co. KGaA, Weinheim

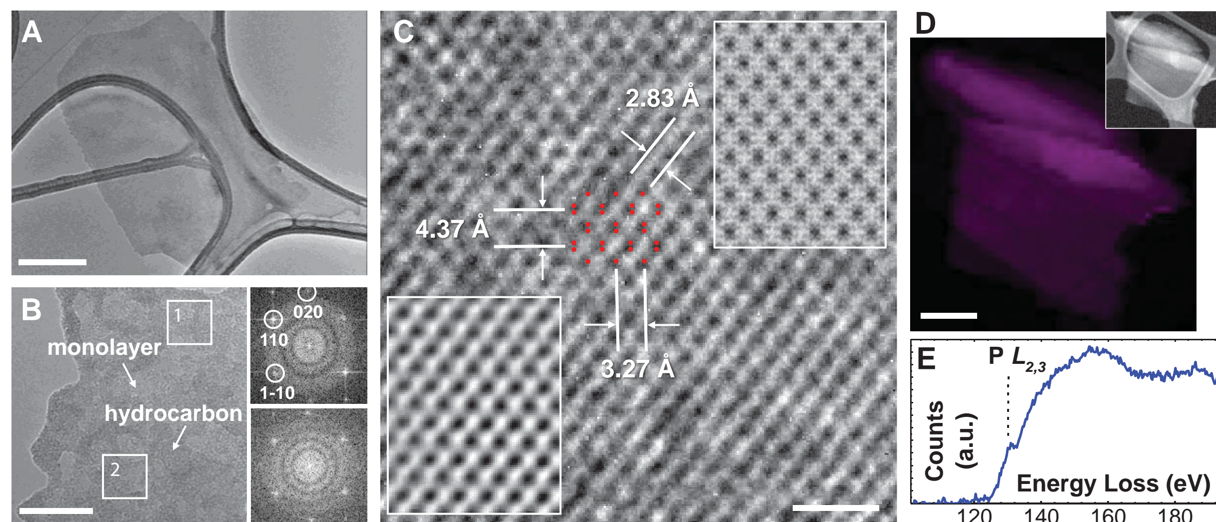

Figure 3. High-resolution TEM and EELS characterizations of BP nanoflakes. A) A typical TEM image of a BP flake on lacy carbon support (scale bar is 200 nm). B) TEM image, as well as FFT of the selected area 1 (upper right) and 2 (lower right), showing monolayer BP covering a region in excess of 80 nm × 80 nm (scale bar is 20 nm). The FFT patterns of different selected areas across the entire flake show identical features, suggesting uniform existence of single layer BP over the entire flake. C) High resolution TEM image of monolayer BP nanoflake taken from a selective area in B (scale bar is 1 nm). TEM simulation (upper right inset) and a filtered section of the acquired image (lower left inset) are added for comparison. The lattice parameters perfectly match the monolayer BP structure. D) EELS map and corresponding high-angle annular dark-field (HAADF) image (upper right inset) of a flake on lacy carbon support (scale bar is 200 nm). Comparison between HAADF and spectrum images shows a pure phosphorous distribution on the flake. Each pixel size of the EELS map is 22 nm. E) An individual EELS spectrum of the EELS map shown in D). Absence of the signature P_xO_y peak loss confirms the pristine phosphorous structure all over the flake. Panels (A), (B), and (D) are taken from different flakes.

versus V_{BG} characteristics of the device (V_{SD} = 0.7 V) the field-effect mobility for holes is calculated to be ≈0.58 cm^2 V^{-1} s^{-1}. The drain current modulation (on/off ratio) in our device is as large as 10^3. As shown in Figure 4C, the *n*-branch starts at V_{BG} = 85 V which is in a good agreement with the previous reports on FETs made of mechanically exfoliated BP flakes in similar gate conditions.[13] The position of minimum conductivity can be shifted down by using thinner gate oxides,[12] and the electron mobility (*n*-branch) can be enhanced using appropriate contact metals.[26] The I_{SD}–V_{SD} characteristics of our devices (provided in Section S5, Supporting Information) show a non-Ohmic behavior, attributed to trap states and solvent residues.[27] The Schottky barrier and large contact resistances are mainly responsible for the lower mobility values compared with mechanically exfoliated BP FETs. Such transistors do not often get to their saturation regime since a large portion of the applied V_{SD} drops across the contact resistances.[12]

In summary, we have demonstrated large scale production of highly crystalline and pure BP nanoflakes via liquid-phase exfoliation, where the dispersed flakes are well protected against degradation in the solution form. The exfoliated nanoflakes show competitive electrical properties to mechanically exfoliated BP flakes. This work opens up new possibilities for the BP atomic layers to be formed into thin films and composites in large scales with a wide range of applications such as flexible electronics and optoelectronics,[1,28,29] energy generation and storage systems,[30] catalysis,[31,32] chemical-[33] and biosensing,[2] etc.

During the revision process of this paper we noted that an experimental paper on liquid- phase exfoliation of BP was published.[34]

Experimental Section

Sample Preparation: Bulk black phosphorous (purchased from Smart Elements) of ≈0.2 mg was immersed in 10 mL of solutions in the form of either a single chunk, or a ground powder. The prepared samples were sonicated in a Sonics Vibra-Cell sonicator (130 W) for an appropriate time (see Section S3, Supporting Information for the optimization process). Afterward, the solution was centrifuged in an Eppendorf 5424 Centrifugation machine (250 W) for 30 min in 2000 rpm and the top 50% of the solution was collected and filtered using a Sigma–Aldrich vacuum filtration assembly on a polytetrafluoroethylene (PTFE) membrane filter of 0.1 µm pore size. The filtered film was then thoroughly washed many times by ethanol, water, and isopropyl alcohol (IPA) to remove the solvent residue. The stacked flakes were then dispersed in IPA. The solution was drop cast on degenerately doped Si substrate with 270 nm thermally grown SiO_2 using polyethylene pipette and dried under light (or on a hotplate at 90 °C). The samples were then gently rinsed in methanol, deionized (DI) water, and IPA and N_2 blown to remove the solvent residues in the evaporation stage.

UV–vis–IR Spectroscopy: UV–vis–NIR spectroscopy was performed using a Perkin–Elmer LAMBDA 1050 high-performance UV/Vis/NIR double-beam spectrophotometer. This machine covers the wavelength range of 185–3300 nm using three detectors (photomultiplier R6872, three-stage wide-band Peltier cooled InGaAs and single-stage Peltier cooled PbS). We mainly focused on the NIR range using the InGaAs detector, which covers the range of (≈830 to ≈2400 nm).

DLS: DLS was carried out at 25 °C using a DLS unit from Brookhaven Instruments, which consists of a Brookhaven BI-200 goniometer and BI-9000 high-speed correlator and a 3 W argon-ion laser operating at 514 nm. The volume of the samples was 50 µL. All the samples were cleared of any air bubbles before measurement. The correlated nanoflake size was measured based on calculated base line with a 1–5% error.

SEM: SEM was performed using a Carl–Zeiss electron microscope integrated in a Raith e-LiNE plus electron-beam lithography system. The

© 2015 WILEY-VCH Verlag GmbH & Co. KGaA, Weinheim

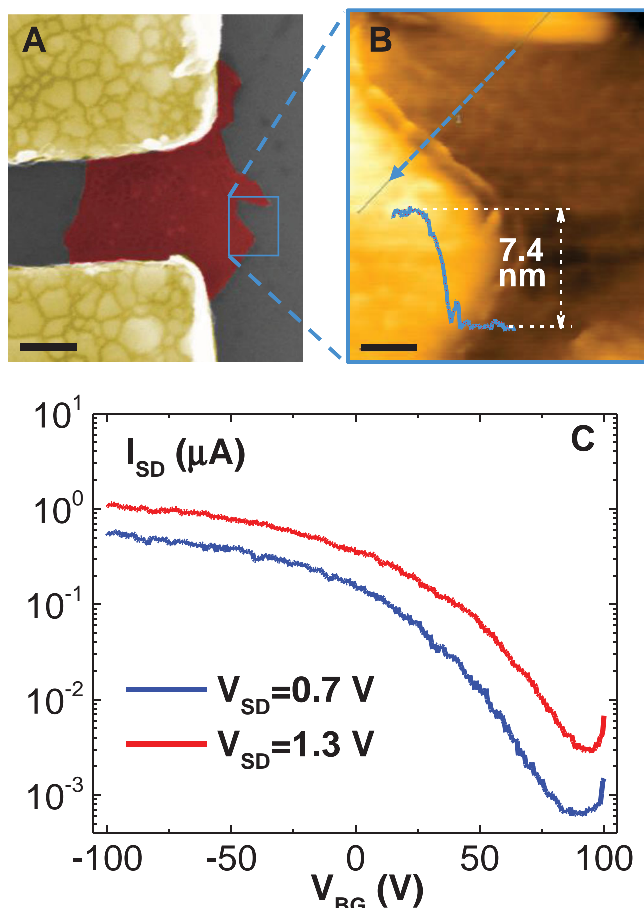

Figure 4. Electrical characterization of individual flake FETs and centimeter scale thin film. A) False color SEM image of an individual few layers thick BP FET. The scale bar is 200 nm. B) AFM image of selected region of Figure 4A. Line profile corresponding to drawn line (blue) shows height (7.4 nm) of the nanoflake. The scale bar is 50 nm. C) Source–drain current (I_{SD}) with respect to the applied back gate voltage (V_{BG}) swept from −100 to +100 V. The source-drain bias (V_{SD}) is 0.7 and 1.3 V for the black and red curves, respectively.

images were acquired at 20 kV acceleration voltage and with a 30 μm aperture size.

AFM: AFM was performed on drop-cast flakes on Si/SiO_2 substrates using an Icon Bruker system in standard tapping mode. It was tried to minimize the time between sample preparation and AFM experiments in order to reduce the degradation of the flakes.

Raman Spectroscopy: The polarization/orientation Raman measurements of the liquid exfoliated flakes were performed using a HORIBA XploRA instrument. The excitation wavelength was 532 nm with 1.0 mW focused on individual flakes of phosphorene using a 100× microscope objective. Data were collected without a Raman analyzer.

Samples were mounted on a rotational stage with 15° rotational gradations. The BP nanoflakes that appeared the most uniform based upon their color when viewed with white reflected light were selected for polarization/orientation Raman analysis. This was done to avoid convolution of spatially varying structural contributions to the spectra as the sample's orientation with respect to the incident laser polarization was varied. Spectra were collected in 15° rotational increments from 0° to 180° with respect to the laboratory frame.

TEM: The exfoliated flakes were characterized in the aberration-corrected JEOL ARM200CF scanning TEM (STEM)/TEM operated at electron energy of 80 keV to minimize damage caused by the electron beam. The microscope was equipped with a cold field-emission source, which yielded 0.35 eV energy resolution and 1.2 Å spatial resolution with the probe spherical-aberration corrector in STEM mode, and 2 Å resolution in TEM mode. A convergence semiangle of 16.5 mrad was used for both STEM imaging and EELS. For HAADF-STEM imaging, a 90 mrad collection inner angle was used. For EELS, a collection semiangle of 71 mrad was used. A digital micrograph (Gatan, Inc., USA) was utilized for all data acquisition. For sample preparation, the dispersed nanoflakes in IPA were drop-cast on a lacey-carbon TEM grid. The samples were then lamped for 15 min to dry out the solvent and immediately loaded into the microscope. High-resolution TEM images of both mono- and multilayer BP were simulated using Kirkland multislice code[35] using the following TEM parameters: incident beam energy: 80 keV; thermal vibration temperature: 300 K; spherical aberration C_s: 0.5 mm; defocus for single layer: 30 Å; defocus for multilayer: 48 Å; objective aperture size: 500 mrad.

Device Fabrication and Electrical Measurements: The samples were prepared using the drop-casting technique and were immediately annealed at 200 °C for 2 h in vacuum to remove the excess residue and increase the adhesion of the flakes to the substrate. This step is essential to reduce the contact resistance. The samples were then immediately coated with a poly(methyl methacrylate) (PMMA) double layer and the electrode patterns were carried out in an electron-beam lithography (EBL) process. Immediately after developing, the samples were loaded in a metal evaporation vacuum chamber and 15 nm of titanium followed by 85 nm of gold were deposited. The samples were annealed again in vacuum at 200 °C for 2 h to remove fabrication residues. The samples were always kept in a vacuum except during the electrical characterizations. The electrical performance of the devices was monitored using Keithley 2612A source-meter in two-probe configuration. All the electrical measurements were carried out in ambient conditions.

Supporting Information

Supporting Information is available from the Wiley Online Library or from the author.

Acknowledgements

B.K. and T.F. contributed equally to this work. A.S.-K., P.Y., B.K., T.F. conceived the idea. A.S.-K. led the material synthesis, fabrication, characterizations (except TEM), and experiments. R.F.K. led the TEM analysis and imaging. T.F., B.K., and M.A. performed the liquid exfoliation and absorption spectroscopy experiments. M.A. performed DLS. P.Y. performed SEM, AFM, device fabrication, and electrical characterizations. D.T. and P.Y. performed Raman spectroscopy experiments. C.W. performed TEM imaging and analysis. A.S.K. and J.E.I. jointly supervised T.F. All the authors contributed to manuscript preparation and discussions. A.S.-K.'s work was supported by the University of Illinois at Chicago through the Startup budget. The acquisition of the UIC JEOL JEM-ARM200CF is supported by a MRI-R2 grant from the National Science Foundation [DMR-0959470]. The authors acknowledge the MRSEC Materials Preparation and Measurement Laboratory shared user facility at the University of Chicago (Grant No. NSF-DMR-1420709).

Received: November 10, 2014
Revised: December 26, 2014
Published online: February 2, 2015

[1] K. S. Kim, Y. Zhao, H. Jang, S. Y. Lee, J. M. Kim, K. S. Kim, J.-H. Ahn, P. Kim, J.-Y. Choi, B. H. Hong, *Nature* **2009**, *457*, 706.
[2] Y. Shao, J. Wang, H. Wu, J. Liu, I. A. Aksay, Y. Lin, *Electroanalysis* **2010**, *22*, 1027.

© 2015 WILEY-VCH Verlag GmbH & Co. KGaA, Weinheim

[3] B. Kumar, K. Min, M. Bashirzadeh, A. B. Farimani, M.-H. Bae, D. Estrada, Y. D. Kim, P. Yasaei, Y. D. Park, E. Pop, N. R. Aluru, A. Salehi-Khojin, *Nano Lett.* **2013**, *13*, 1962.
[4] O. Lopez-Sanchez, D. Lembke, M. Kayci, A. Radenovic, A. Kis, *Nat. Nanotechnol.* **2013**, *8*, 497.
[5] K. S. Novoselov, V. I. Fal'ko, L. Colombo, P. R. Gellert, M. G. Schwab, K. Kim, *Nature* **2012**, *490*, 192.
[6] Q. H. Wang, K. Kalantar-Zadeh, A. Kis, J. N. Coleman, M. S. Strano, *Nat. Nanotechnol.* **2012**, *7*, 699.
[7] A. K. Geim, K. S. Novoselov, *Nat. Mater.* **2007**, *6*, 183.
[8] J.-H. Chen, C. Jang, S. Xiao, M. Ishigami, M. S. Fuhrer, *Nat. Nanotechnol.* **2008**, *3*, 206.
[9] T. H. Wang, Y. F. Zhu, Q. Jiang, *J. Phys. Chem. C* **2013**, *117*, 12873.
[10] B. Radisavljevic, A. Radenovic, J. Brivio, V. Giacometti, A. Kis, *Nat. Nanotechnol.* **2011**, *6*, 147.
[11] M. S. Fuhrer, J. Hone, *Nat. Nanotechnol.* **2013**, *8*, 146.
[12] H. Liu, A. T. Neal, Z. Zhu, Z. Luo, X. Xu, D. Tománek, P. D. Ye, *ACS Nano* **2014**, *8*, 4033.
[13] F. Xia, H. Wang, Y. Jia, *Nat. Commun.* **2014**, *5*, 4458.
[14] L. Li, Y. Yu, G. J. Ye, Q. Ge, X. Ou, H. Wu, D. Feng, X. H. Chen, Y. Zhang, *Nat. Nanotechnol.* **2014**, *9*, 372.
[15] S. Das, W. Zhang, M. Demarteau, A. Hoffmann, M. Dubey, A. Roelofs, *Nano Lett* **2014**, *14*, 5733.
[16] V. Tran, R. Soklaski, Y. Liang, L. Yang, *Phys. Rev. B* **2014**, *89*, 235319.
[17] J. Qiao, X. Kong, Z.-X. Hu, F. Yang, W. Ji, *Nat. Commun.* **2014**, *5*, 4475.
[18] V. Tran, R. Soklaski, Y. Liang, L. Yang, *Phys. Rev. B* **2014**, *89*, 235319.
[19] A. Favron, E. Gaufrès, F. Fossard, P. L. Lévesque, A.-L. Phaneuf-L'Heureux, N. Y. Tang, A. Loiseau, R. Leonelli, S. Francoeur, R. Martel, **2014**, arXiv:1408.0345 [cond-mat.mes-hall]; available from: http://arxiv.org/abs/1408.0345.
[20] S. P. Koenig, R. A. Doganov, H. Schmidt, A. H. Castro Neto, B. Özyilmaz, *Appl. Phys. Lett.* **2014**, *104*, 103106.
[21] A. Castellanos-Gomez, L. Vicarelli, E. Prada, J. O. Island, K. L. Narasimha-Acharya, S. I. Blanter, D. J. Groenendijk, M. Buscema, G. a Steele, J. V Alvarez, H. W. Zandbergen, J. J. Palacios, H. S. J. van der Zant, *2D Mater.* **2014**, *1*, 025001.
[22] S. Zhang, J. Yang, R. Xu, F. Wang, W. Li, M. Ghufran, Y.-W. Zhang, Z. Yu, G. Zhang, Q. Qin, Y. Lu, *ACS Nano* **2014**, *8*, 9590.
[23] C.-J. Shih, A. Vijayaraghavan, R. Krishnan, R. Sharma, J.-H. Han, M.-H. Ham, Z. Jin, S. Lin, G. L. C. Paulus, N. F. Reuel, Q. H. Wang, D. Blankschtein, M. S. Strano, *Nat. Nanotechnol.* **2011**, *6*, 439.
[24] X. Wang, A. M. Jones, K. L. Seyler, V. Tran, Y. Jia, H. Zhao, H. Wang, L. Yang, X. Xu, F. Xia, **2014**, arXiv:1411.1695 [cond-mat.mes-hall]; available from: http://arxiv.org/abs/1411.169.
[25] R. Hultgren, N. S. Gingrich, B. E. Warren, *J. Chem. Phys.* **1935**, *3*, 351.
[26] S. Das, M. Demarteau, A. Roelofs, *ACS Nano* **2014**, *8*, 11730.
[27] J. N. Coleman, M. Lotya, A. O'Neill, S. D. Bergin, P. J. King, U. Khan, K. Young, A. Gaucher, S. De, R. J. Smith, I. V Shvets, S. K. Arora, G. Stanton, H.-Y. Kim, K. Lee, G. T. Kim, G. S. Duesberg, T. Hallam, J. J. Boland, J. J. Wang, J. F. Donegan, J. C. Grunlan, G. Moriarty, A. Shmeliov, R. J. Nicholls, J. M. Perkins, E. M. Grieveson, K. Theuwissen, D. W. McComb, P. D. Nellist, V. Nicolosi, *Science* **2011**, *331*, 568.
[28] Y. Xu, H. Bai, G. Lu, C. Li, G. Shi, *J. Am. Chem. Soc.* **2008**, *130*, 5856.
[29] S. Xu, Y. Zhang, L. Jia, K. E. Mathewson, K.-I. Jang, J. Kim, H. Fu, X. Huang, P. Chava, R. Wang, S. Bhole, L. Wang, Y. J. Na, Y. Guan, M. Flavin, Z. Han, Y. Huang, J. A. Rogers, *Science* **2014**, *344*, 70.
[30] J. Xiao, D. Choi, L. Cosimbescu, P. Koech, J. Liu, J. P. Lemmon, *Chem. Mater.* **2010**, *22*, 4522.
[31] B. Kumar, M. Asadi, D. Pisasale, S. Sinha-Ray, B. A. Rosen, R. Haasch, J. Abiade, A. L. Yarin, A. Salehi-Khojin, *Nat. Commun.* **2013**, *4*, 1.
[32] M. Asadi, B. Kumar, A. Behranginia, B. A. Rosen, A. Baskin, N. Repnin, D. Pisasale, P. Phillips, W. Zhu, R. Haasch, R. F. Klie, P. Král, J. Abiade, A. Salehi-Khojin, *Nat. Commun.* **2014**, *5*, 4470.
[33] A. Salehi-Khojin, D. Estrada, K. Y. Lin, K. Ran, R. T. Haasch, J.-M. Zuo, E. Pop, R. I. Masel, *Appl. Phys. Lett.* **2012**, *100*, 033111.
[34] J. R. Brent, N. Savjani, E. A. Lewis, S. J. Haigh, D. J. Lewis, P. O'Brien, *Chem. Commun. (Cambridge U.K.)* **2014**, *50*, 13338.
[35] E. J. Kirkland, *Advanced Computing in Electron Microscopy*, Springer US, Boston, MA, USA **2010**.

© 2015 WILEY-VCH Verlag GmbH & Co. KGaA, Weinheim